JET–P(99)43

C F Maggi et al

The Effect of Charge Exchange with Neutral Deuterium on Carbon Emission in JET Divertor Plasmas

JET–P(99)43

The Effect of Charge Exchange with Neutral Deuterium on Carbon Emission in JET Divertor Plasmas

C F Maggi, L D Horton, H P Summers[1].

JET Joint Undertaking, Abingdon, Oxfordshire, OX14 3EA,
[1]Physic and Applied Physics Department, University of Strathclyde, Glasgow, UK.

Preprint of a Paper to be submitted for publication in
PlasmaPhysics and Controlled Fusion

November 1999

ABSTRACT

High density, low temperature divertor plasma operation in tokamaks results in large neutral deuterium concentrations in the divertor volume. In these conditions, low energy charge transfer reactions between neutral deuterium and the impurity ions can in principle enhance the impurity radiative losses and thus help to reduce the maximum heat load to the divertor target. A quantitative study of the effect of charge exchange on carbon emission is presented, applied to the JET divertor. Total and state selective effective charge exchange recombination rate coefficients were calculated in the collisional radiative picture. These coefficients were coupled to divertor and impurity transport models to study the effect of charge exchange on the measured carbon spectral emission in JET divertor discharges. The sensitivity of the effect of charge exchange to the assumptions in the impurity transport model was also investigated. A reassessment was made of fundamental charge exchange cross section data in support of this study.

1. INTRODUCTION

In ionization equilibrium charge exchange recombination modifies the carbon power loss function by shifting the radiative losses from the lower charge states towards higher temperatures. For this reason it is expected that, especially in high density, detached divertor plasmas, characterized by large neutral deuterium concentrations in the divertor volume (n_D/n_e up to ~10%), charge transfer reactions will enhance the carbon radiative losses, thereby reducing the maximum heat load to the divertor target tiles.

However, local, stationary ionization equilibrium does not apply to divertor plasmas, since the characteristic time scales for parallel transport of impurity ions and for recycling of hydrogen neutrals are much shorter than the time scales to reach ionization equilibrium. For this reason, we have embedded low energy charge transfer in divertor impurity transport modelling for the study of this process in JET discharges. Direct charge exchange population of the excited levels of the partially stripped ions (C II - C IV are the key carbon radiators in JET divertor plasmas [1]) competes with population by electron impact excitation from the ground and low lying metastable states of these ions. At the low collision energies typical of divertor plasmas, the charge transfer reactions are strongly state selective and so enhance only certain spectral line emissivities. Suitable line ratios can then in principle lead to measurement of the hydrogen concentration. The fundamental data requirement here is therefore not only total charge exchange cross sections but also state selective cross sections.

In the collisional-radiative calculation of the present work, we have derived total and state selective effective charge exchange recombination rate coefficients for all carbon ions. These have been included in the *Atomic Data and Analysis Structure* (ADAS) package [2]. The fundamental low energy charge exchange data preparation required a detailed reassessment and review. This is given in Section A.

2. CALCULATION OF THE COLLISIONAL-RADIATIVE CHARGE EXCHANGE RATE COEFFICIENTS

Using the charge exchange cross sections reviewed in Appendix A we have calculated a complete set of stage to stage rate coefficients for carbon, as required for the evaluation of the carbon ionization balance. In our calculations the donor species is deuterium, which is the most relevant isotope for present fusion experiments. We have assumed that electron capture cross sections from a deuterium donor are equal to those from a hydrogen donor for the same collision speed. Because of the low collision energies in cold divertor plasmas and due to the similar masses of donor and receiver particles, the velocities of both reacting particles may be comparable. The rate coefficients are then properly obtained by averaging over the velocity distribution functions of both particle species as:

$$< \sigma v > \; = \int\int f_D(\vec{v}_D)\, f_C(\vec{v}_C) |\vec{v}_D - \vec{v}_C| \sigma(|\vec{v}_D - \vec{v}_C|)\, d^3\vec{v}_D\, d^3\vec{v}_C \qquad (1)$$

where σ is the electron capture cross section, $|\vec{v}_D - \vec{v}_C|$ is the relative collision speed between the donor (neutral deuterium) and the receiver (C^{+z} ion) and $f_D(\vec{v}_D)$, $f_C(\vec{v}_C)$ are the velocity distribution functions of the donor and receiver species respectively (here the subscript C denotes a generic C^{+z} ion).

In the calculation of the rate coefficients we have allowed two different distribution functions, Maxwellian and monoenergetic for both donor and receiver. Rate coefficients can be generated for any combination of the distribution functions of both particles. However, for the study in this paper, the rate coefficients were double Maxwellian averages with equal donor and receiver temperatures ($T_D = T_C$). Fig. 1 illustrates the total charge exchange rate coefficients for carbon ions.

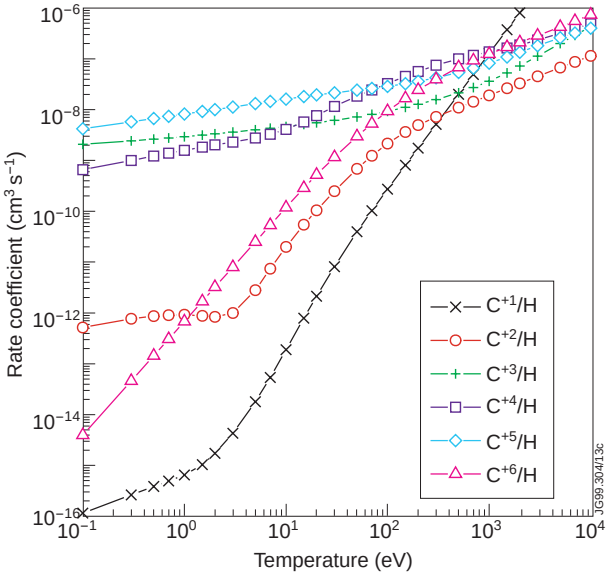

Figure 1. Total charge exchange rate coefficients for carbon ions. The donor isotope is deuterium and the calculation assumes double Maxwellian averages for equal donor and receiver temperatures $T_D = T_C$.

From a spectroscopic point of view, the intensity of a spectral line, $I_{i\rightarrow j}$ emitted in the transition from upper level *i* to lower level *j* of an ion C^{+z} is given by:

$$I_{i\rightarrow j} = 1/4\pi \int_{LOS} \varepsilon_{i\rightarrow j}\, dl \qquad (2)$$

where the integral is over the spectrocopic line of sight (LOS) through the plasma, and $\varepsilon_{i\rightarrow j}$ is the volume photon emissivity, with $\varepsilon_{i\rightarrow j} = n_i A_{i\rightarrow j}$, where n_i is density of level *i* and $A_{i\rightarrow j}$ is the

Einstein coefficient. From the collisional-radiative excited state population calculation, the volume photon emission is obtained in terms of effective photon emissivity coefficients q^{eff} as

$$\varepsilon_{i\to j} = \sum_{\rho} n_e n_\rho^z q_{\rho,\, i\to j}^{eff,exc} + \sum_{\tau} (n_e n_\tau^{z+1} q_{\tau,\, i\to j}^{eff,rec} + n_H n_\tau^{z+1} q_{\tau,\, i\to j}^{eff,cx}) \qquad (3)$$

where ρ, τ label metastable states (including the ground state) of the ion of charge state *z* and *z*+1, respectively, $q^{eff,exc}$, $q^{eff,rec}$ and $q^{eff,cx}$ are the photon emissivity coefficients for electron impact excitation, free electron recombination and charge exchange with neutral hydrogen and n_e, n_H and n^z are the densities of electrons, hydrogen and impurities of charge *z*, respectively. This formulation is particularly suited to transport studies, since it allows the expression of the spectral intensities in terms of the product of the densities of the dominant species (described by the transport equations) and of atomic coefficients dependent only on local plasma parameters. Note that the coefficients $q^{eff,exc}$ etc are collisional-radiative coefficients depending on density as well as temperature.

We have derived charge exchange photon emissivity coefficients $q^{eff,cx}$ for a large number of spectrocopic lines for each carbon charge state. This excludes C^{+0}, due to the lack of state selective charge exchange cross sections for the reaction C^{+1}/H (see section A.1). As an example, Fig. 2 shows $q^{eff,cx}$ for the C IV 3s – 2p spectral line (λ = 419.7 Å).

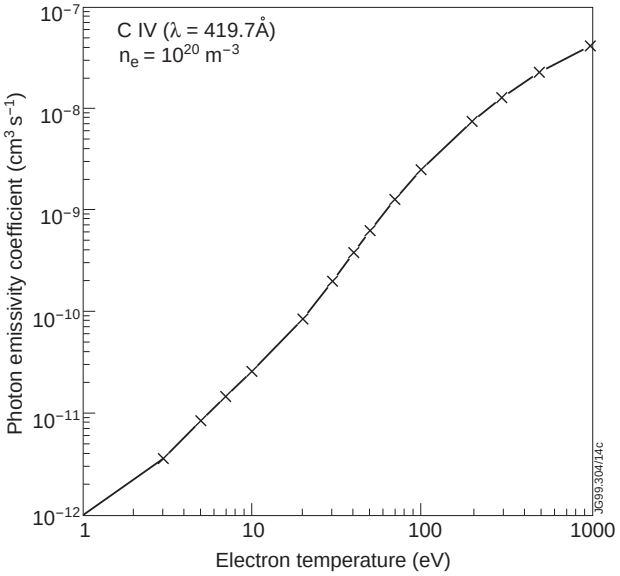

Figure 2. Charge exchange photon emissivity coefficient for C IV (λ = 419.7 Å).

3. CHARGE EXCHANGE IN UNIFORM PLASMAS IN IONIZATION EQUILIBRIUM

As discussed earlier, charge exchange is influential on carbon radiation in divertor plasmas: by direct population of selective excited states of the carbon ion, and by modification of the overall carbon ionization balance.

We consider first the effect of direct population illustrated by the C III spectrum. Only the $2p^2\ ^1S$ and the 2s 3s ^3S states are strongly populated by charge exchange capture in the energy range 1-10 eV, relevant to C III emission in high density JET divertor discharges. The charge exchange process is in competion with electron impact excitation from the ground and metastable level of C^{+2} for dominance of spectral line emission. The spectral line ratio 538.2 Å (2s 3s ^3S – 2s 2p ^3P) to 1175.6 Å ($2p^2\ ^3P$ – 2s 2p ^3P) reflects this competition. For a representative neutral

hydrogen density of $n_D = 0.1 \times n_e$, with $n_e = 10^{20}$ m^{-3}, the contribution of charge exchange to the line ratio is at most 30% at 10 eV. This is below the precision of the available VUV measurements (absolute calibration error ~ 50%) and of the accuracies of the fundamental cross section data. Therefore, in JET divertor plasmas spectral line ratios from the same carbon ion cannot be used to diagnose charge exchange in the same way as they are used for electron temperature and density diagnostics.

The second, more important effect is the modification of the carbon ionization balance by inclusion of charge exchange, which gives

$$\frac{n(C^{+z+1})}{n(C^{+z})} = \frac{S}{\alpha_{rec} + \frac{n_H}{n_e}\alpha_{cx}} \tag{4}$$

where S, α_{rec} and α_{cx} are the effective, stage to stage, ionization, recombination and charge exchange rate coefficients. This, in turn, affects the total radiated power. Following ref. [3], we define the carbon power loss function, P(C) [Wm^3] by

$$P_{RAD} = n_e\, n(C)\, P(C) \tag{5}$$

where P_{RAD} [Wm^{-3}] is the power radiated per unit volume by the impurity, n_e the electron density and n(C) is the total carbon density. Thus

$$P(C) = \sum_{z=0}^{Z_0} \frac{n(C^{+z})}{n(C)} P(C^{+z}) \tag{6}$$

and is the sum of the individual contributions from each charge state. Z_0 is the nuclear charge and $n(C^{+z})/n(C)$ the C^{+z} fractional abundance, with

$$n(C) = \sum_{z=0}^{Z_0} n(C^{+z}). \tag{7}$$

The equilibrium radiated power function for carbon is shown in Fig.3 without charge exchange ($n_D = 0$) and with charge exchange at two hydrogen concentrations, 1% and 10%. The latter represents an upper value found when modelling high density JET divertor plasmas. We assume $T_D = T_e$.

The equilibrium radiated power function increases markedly at higher temperatures with inclusion of charge exchange. At 100 eV P(C) is increased by one order of magnitude for n_D/n_e = 1%. This is due to the increase of the fractional abundance of C^{+3} which is lithium-like and a very efficient radiator compared with C^{+4}. With increasing hydrogen concentration, the lower charge states emitting at lower temperature are also affected. The C III radiated power increases more than one order of magnitude at 100 eV when n_D/n_e increases from 1 to 10%. In the temperature range 1 - 10 eV, most typical in high density JET divertor plasmas, the increase of

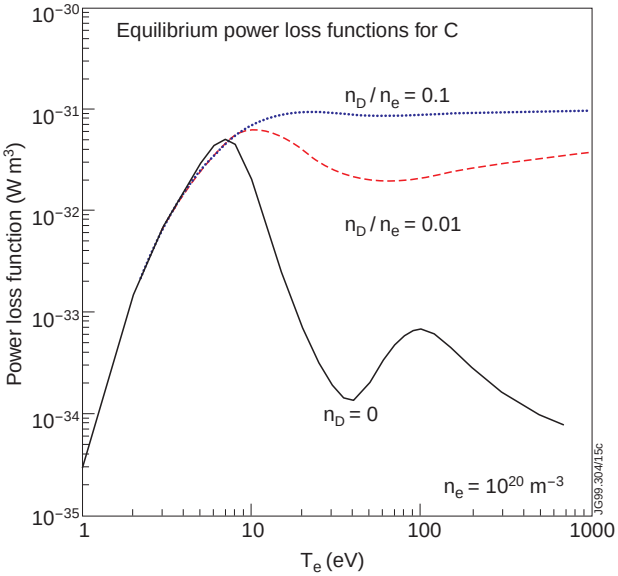

Figure 3. Equilibrium power loss functions for carbon with and without charge exchange.

P(C) is more modest, but there is a change in the main radiators, with C III gradually becoming dominant. $P(C^{+2})$ broadens in this temperature range as n_D/n_e increases. Thus, for uniform plasma in ionization equilibrium, the main influnce of charge exchange recombination is the enhancement of the total carbon radiation due to the shift of the ionization balance to less ionized (and thus more radiative) charge state distributions.

4. CHARGE EXCHANGE IN THE PRESENCE OF DIVERTOR PLASMA TRANSPORT

In the divertor and scrape-off-layer (SOL) plasma, transport both in the direction parallel to the magnetic field and in the radial direction across the magnetic field is important. Models of this region therefore require at least a 2-D approach. In addition, since the impurity and plasma species (fluids) are coupled, a self-consistent treatment of the impurity and hydrogenic plasma transport is necessary. At present, 2-D fluid models are most suited to divertor studies which seek to be both interpretative and predictive. At JET the main 2-D fluid code EDGE2D is operated in an iterative coupling with NIMBUS [4], a 2-D Monte Carlo code for the neutral plasma species.

4.1 Introduction to the 2-D Model

The electrons and hydrogenic and impurity ion species are described by a set of fluid equations for conservation of particles, momentum and energy. Toroidal symmetry is assumed and the fluid equations are solved in the poloidal plane, with components parallel and perpendicular to the magnetic field lines. Parallel transport is assumed to be classical and the equations for parallel transport follow Braginskii's formulation [5]. Cross field transport is assumed to be diffusive, with anomalous transport coefficients.

The main boundary conditions which are prescribed are the power that crosses the magnetic separatrix from the confined plasma (including the proportion shared between electrons and ions) and the plasma density at the separatrix - generally at the plasma outer midplane. Also the anomalous perpendicular diffusion coefficients for the transport of particles ($D_\perp$) and electron and ion energy ($\chi_{e,\perp}$ and $\chi_{i,\perp}$) are specified as input parameters.

The fluid equations are solved on a 2-D mesh based on a poloidal projection of the flux surfaces generated from the calculated magnetic equilibrium for the discharge. Additional information on the material structures inside the vacuum chamber (such as the specific geometry of the divertor targets), which affect the transport of the neutrals in the region between plasma and vessel walls, can be associated with the boundary cells of the mesh.

4.2. Simulation of JET Divertor Discharges

We consider an ohmically heated discharge, in which the plasma density was raised steadily to the density limit by deuterium gas fuelling in the divertor chamber. Fig. 4 shows the main plasma parameters of the discharge.

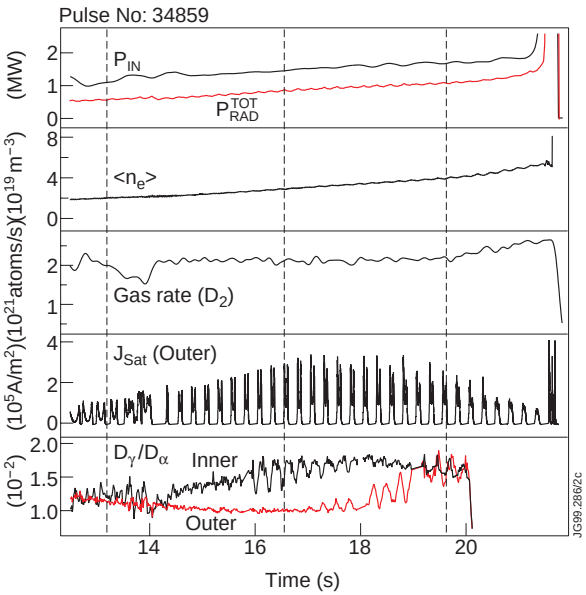

Figure 4. Overview of the main plasma parameters of the Ohmic density limit discharge used in the simulations: total input and radiated power, line averaged density, gas fuelling rate, separatrix ion saturation current to outer divertor target measured by Langmuir probes (note the 4 Hz strike point sweeping) and Dγ/Dα spectroscopic line ratios at the inner and outer divertor targets.

As the mean core plasma density, $<n_e>$, increases the ion saturation current to the divertor target, J_{sat}, measured by an array of Langmuir probes, firstly increases supra-linearly with $<n_e>$ (the high recycling regime) and then begins to fall as the density increases further. The divertor Dα emission and neutral pressure, however, continue to increase (not shown), while J_{sat} decreases to very low values (first in the inner and then in the outer divertor). This is the signature of plasma detachment [6]. As the divertor radiation increases, its spatial maxima move from near the target to the X-point region. When the density is increased further, a MARFE forms, which enters the confined plasma and provokes a density limit disruption. In the discharge of Fig. 4 the strike points were swept back and forth at 4 Hz across the target plates to spread the power load to the target surface. The signature of the sweeping is seen clearly in the J_{sat} signal.

With increasing main plasma density, the divertor density increases and the divertor temperature decreases to very low values. At detachment, the Langmuir probes measure values of T_e ~ 2-5 eV, which however overestimate T_e, since the standard interpretation of the probe I-V characteristic does not apply in this regime [7]. Spectroscopic line ratio measurements of Dγ/Dα emission in the divertor (shown in the bottom box of Fig. 4 for this discharge) indicate temperatures of order $\leq$1-2 eV at detachment [8].

Also with increasing plasma density, the divertor neutral deuterium density increases and thus the effect of charge exchange is expected to be strongest at high density. We investigate firstly therefore the sensitivity of charge exchange emission to plasma density. Then we examine

the sensitivity of charge exchange to alterations in the plasma transport assumptions.

The simulations are compared with measured line-of-sight emission in the DI and C II – C IV spectra. The time points selected for the simulations are indicated by the dashed vertical lines in Fig. 4. C^{+1} - C^{+3} are the dominant radiating charge states of carbon in the JET divertor [1]. Fig. 5 shows the poloidal cross section of the magnetic equilibrium reconstruction for the discharge with the LOS of the spectrometers overlayed. A double SPRED spectrometer (equipped with 450 g/mm and 2105 g/mm gratings) monitors spectral line emission between 180 and 1450 Å along a vertical LOS directed at the inner target and through the X-point. The VUV spectrometer has a spatial resolution of about 13 cm poloidally at the divertor target and was absolutely calibrated *in situ* using branching ratio techniques [9]. The absolute calibration has an uncertainty of 50%. A CCD camera equipped with an interference filter for Dα provides poloidal profiles across the divertor with 2.5 mm resolution at the target. Visible line emission from DI, C II-IV along integrated views of the inner and outer divertor plasmas are available from photomultiplier tubes coupled to interference filters (for Dα and C III, 4650 Å) and from a Czerny-Turner spectrometer (for Dγ, C II and C IV line emission). The radiated power flux is measured by a vertical bolometer camera with 14 channels covering the whole plasma cross section.

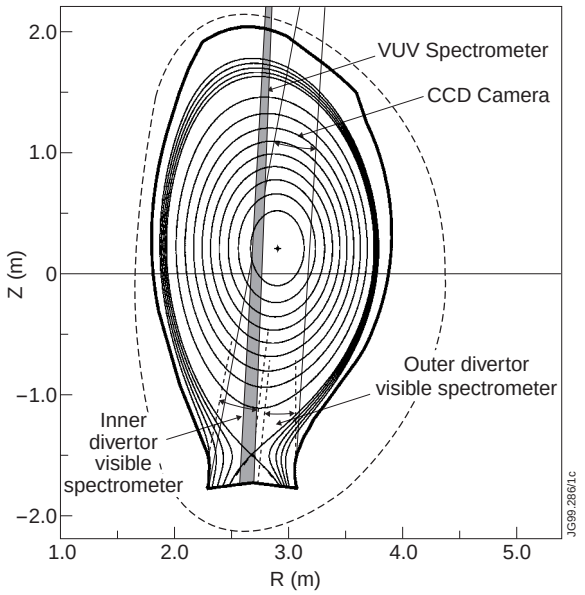

Figure 5. Viewing lines of the spectroscopic diagnostics used in the comparison with the simulated emissivities: double SPRED (grey vertical LOS); CCD camera with interference filters for Dα emission; Dα, Dγ and visible C II-IV integrated line emission from the inner and outer divertor plasmas.

4.2.1. Density Scan

We performed a series of code runs to steady state in which the upstream separatrix density, n_s, was progressively increased. The separatrix density is not routinely measured in JET discharges, but analysis of reciprocating probe data in these regimes shows that a good assumption is $n_s = 0.5 \times \langle n_e \rangle$, where $\langle n_e \rangle$ is the central line averaged density. Thus we set n_s = 1, 1.5 and 2 x 10^{19} m^{-3} for the three time slices of Fig. 4. The input power crossing the separatrix is chosen to be P_{IN} = 1.4 MW at low and medium density and is increased to 1.6 MW at plasma detachment to match the experiment. P_{IN} is divided equally between electron and ion channel. The perpendicular transport coefficients were assumed to be constant, with $D_\perp$ = 0.1 m^2/s (both for deuterons and impurity ions) and $\chi_{e,\perp} = \chi_{i,\perp}$ = 1.5 m^2/s. This choice of transport coefficients allowed us to reproduce the ion flux profile to the target measured by the Langmuir probes in all three density regimes. Carbon production is by physical and chemical sputtering. We used the

physical sputtering yields given by Eckstein et al. [10], together with a constant offset, which approximates a chemically sputtered carbon source. We took this offset equal to 2% at low and medium density and reduced it to 1% at detachment, following the experimental observations that the carbon yield is seen to decrease at low plasma temperature.

Fig. 6 shows the experimental time traces of deuterium line emission, Dα and Dγ and Lyα, Lyβ together with the simulations, marked with the (+) symbol. It can be seen that with increasing density a discrepancy is found between the measured and simulated Balmer and Lyman emission.

Experimentally, the ratio of Dγ/Dα line emission can be used to identify the onset of electron-ion recombination in the divertor volume, which is found to be correlated with plasma detachment [8]. Generally, the Dγ/Dα ratio is observed to decrease monotonically in the outer divertor and then suddenly to increase with increasing main plasma density. In the inner divertor the sudden increase of Dγ/Dα occurs at much lower main plasma densities than in the outer divertor, consistent with an earlier onset of detachment. The sudden increase in the Dγ/Dα line ratio marks the onset of recombination. This evolution can be seen clearly in the bottom box of Fig. 4 for the discharge analysed here. In the outer divertor, recombination starts at 18 s. In the simulations, however, the Dα and Dγ emission from the outer divertor is entirely dominated by excitation (96% of total emission for Dα and 74% for Dγ), even at the highest separatrix density. Hence both Dα and Dγ line emission are underestimated in the model at high density. This may be due to too low an electron density profile in the outer divertor, which leads to the absence of recombination emission. In the inner divertor the onset of recombination occurs at 14.2 s. In the simulations, at low density the Dα and Dγ line emission is driven by excitation, consistent with the measurements. At medium density about 50% of the total Dγ emission is due to recombination, whereas the Dα emission is still dominated by excitation. At detachment 70% of Dγ emission and 25% of Dα emission is due to recombination. The Dα emission is underestimated by a factor of 4 (or more), while the Dγ emission matches the experimental value (within the uncertainty in the calibration). Discrepancy between experimental and simulated Lyman emission is also affected by the private flux region. Here the model fails to reproduce the fall-off in J_{sat} measured by the Langmuir probes, but gives too low ion fluxes and consequently too low neutral fluxes in this region.

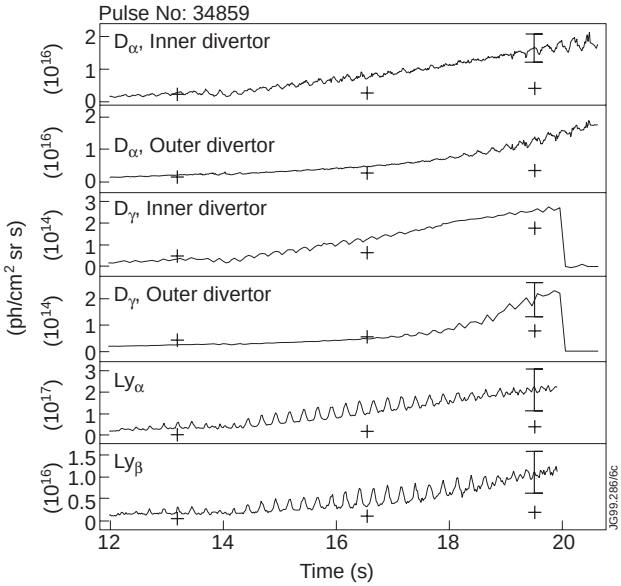

Figure 6. Experimental time traces of deuterium Balmer-α, Balmer-γ and Lyman-α, β line intensities, together with their simulations (+) at the three chosen density values for the discharge of Fig. 4 (note the effect of the strike point sweeping, especially on the VUV signals).

Whereas this profile effect is averaged out for the integrated Dα and Dγ signals, it dominates the Lyman emission simulations, since the VUV spectrometer views a portion of the private flux region with limited spatial resolution (see Fig. 5). Such discrepancies between measured and simulated line integrated emissivities are typical features in the detailed modelling of high density divertor plasma discharges.

In Fig. 7 to 9 we show the comparison between measured and simulated C II-IV divertor spectral line emission in the visible and VUV. The simulations with charge exchange are marked with (+) and those without charge exchange with (*). The agreement between measurements and simulations is generally good, although in some cases outside the experimental error bars given by the uncertainty in the absolute intensity calibration. Some of the predicted line intensity variations with density are not observed experimentally and may arise from incorrect spatial distributions of the line emissivities, especially in the private plasma region.

In Fig. 7 we show visible (inner divertor) and VUV C II line emission. Whereas reasonable agreement is obtained between model and measurements for the visible line at 6785 Å, the simulations overestimate the visible line at 5145 Å and the VUV emission at detachment. The C III line emission at 4650 Å is in good agreement with the measurements (Fig. 8) except at medium density in the inner divertor. The simulated C III VUV spectral lines match well the experiment at low and medium density, but are overestimated in the model at detachment. The theoretical overestimation of C II and C III VUV line emission at high density suggests that the carbon source distribution in the inner divertor, close to the private plasma region, is not correctly described by the 2-D model.

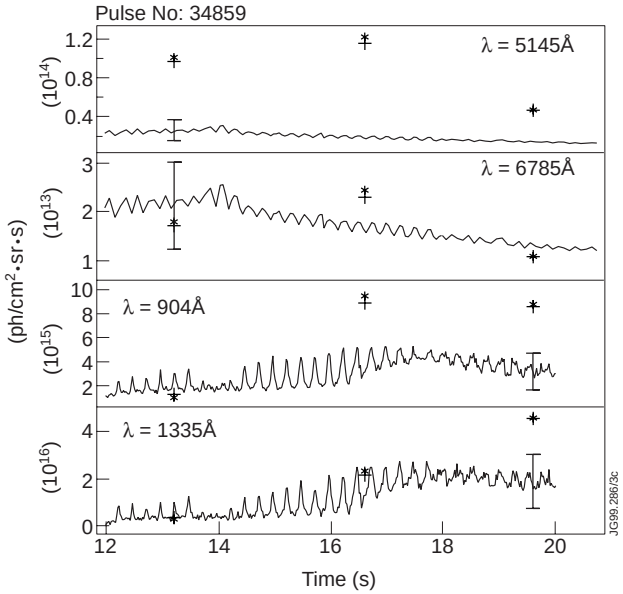

Figure 7. Experimental time traces of C II visible line emission at 5145 Å and 6785 Å for the inner divertor integrated view (similar results apply to the outer divertor) and VUV line emission at 904 Å and 1335 Å, together with their simulations: (+) with charge exchange; (*) without charge exchange.

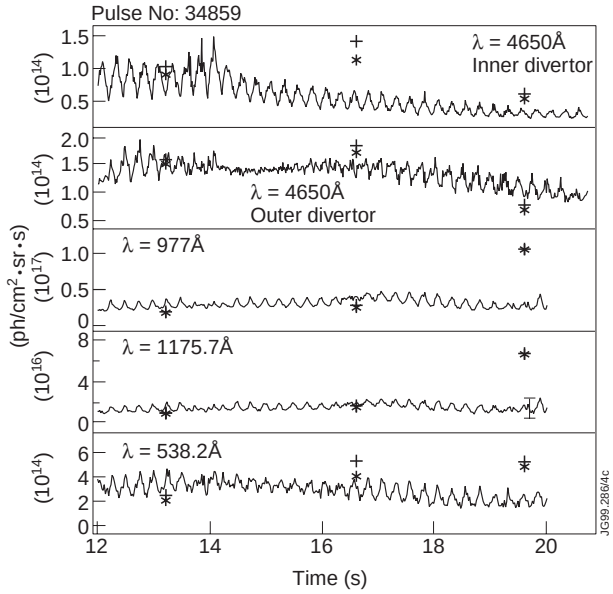

Figure 8. Experimental time traces of C III visible line emission at 4650 Å, for inner and outer integrated divertor views and VUV line emission at 977 Å, 1175.6 Å and 538.2 Å, together with their simulations: (+) with charge exchange; (*) without charge exchange.

This is not surprising since a constant chemical sputtering yield is used to simulate the carbon sources at high density and since the VUV measurements are more sensitive to profile effects due to the narrower spatial resolution of the VUV spectrometer compared to that of the visible system.

The C IV visible line emission (the 3s – 3p doublet at 5810 Å) is underestimated in the simulations by about a factor of 2 to 3 at low density and at detachment, and is in good agreement with the experiment at medium density in the inner divertor (Fig. 9). In the outer divertor it is underestimated in the simulations at all densities. The opposite is found for the VUV lines, for which good agreement with experiment is obtained at low density and detachment, whereas at medium density the model overestimates the line emissivities.

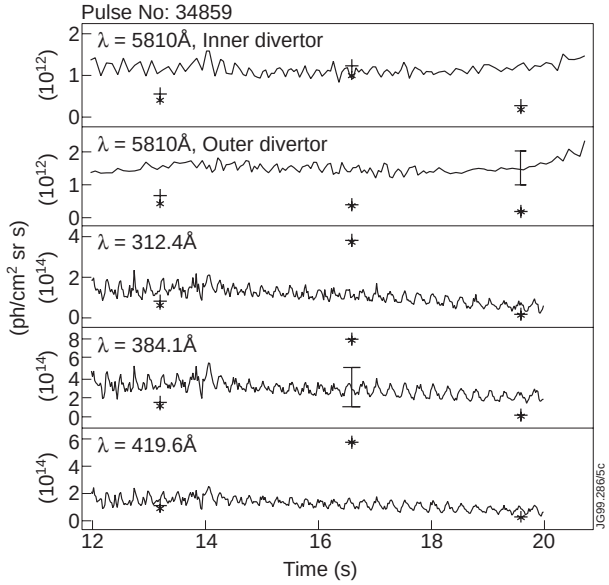

Figure 9. Experimental time traces of the C IV doublet line emission at 5810 Å, for inner and outer integrated divertor views and VUV line emission at 312.4 Å, 384 Å and 419.6 Å, together with their simulations: (+) with charge exchange; (*) without charge exchange.

In summary, for a given separatrix density, it is difficult to obtain a perfect match simultaneously between VUV and visible line emission from the same carbon charge state. This could partly be due to incorrect parallel temperature profiles in the 2-D solutions at high density, which result in the carbon ions radiating at lower temperatures. This enhances emission from lowly excited levels (i.e the VUV emission) and reduces emission from the higher excited levels (typically in the visible range). However, the discrepancy between experimentally measured and simulated line intensities is at most a factor of two outside the experimental error bars. This constitutes quite a satisfactory result bearing in mind the number of different spectral lines and carbon charge states which are modelled simultaneously.

Overall, the C II-IV line emission is found to be weakly sensitive to charge exchange in all density regimes, as can be seen in Fig. 7 through 9. Emission from C II is insensitive to charge exchange, the differences between the simulation with and without charge exchange being of the order of the accuracy of the solution of the fluid equations. This is anticipated, since the rate coefficients for this reaction are rather small (see Fig. 1). In the case of C III, the largest charge exchange cross section is for capture into level 2s 3s ^{3}S, and thus line emission at 538.2 Å is expected to be the most influenced by charge exchange. However, we find at most an increase of 25-30% with charge exchange in this line emission at all densities. Line emission in the 3p ^{3}P – 3s ^{3}S transition at 4650 Å is enhanced by charge exchange by at most 30% at detachment in the inner divertor. This small enhancement in the C III line emission is caused entirely by the change in ionization balance with charge exchange. The direct charge exchange contribution to

the line emission is in fact negligible compared to electron impact excitation. C^{+3} is the charge state mostly affected by charge exchange. In the 3p – 3s transition at 5810 Å it is enhanced by 60% at detachment in the inner divertor and by 40% at low density in the outer divertor (Fig. 9). The C IV line emission is also driven primarily by excitation, although in this case the direct charge exchange contribution reaches a non negligible 30% of the total emission.

This weak sensitivity of the carbon ionization balance on charge exchange can be understood by comparing the characteristic times for ionization, charge exchange and free electron recombination for the different charge states. These times are calculated using the plasma parameters of the actual plasma solution and thus are a function of the transport model. For convenience we consider the variation of the characteristic times along the magnetic field lines and choose the separatrix as representative. For each charge state we compare the times associated with the losses from that charge state, i.e. ionization to the stage above and recombination to the stage below.

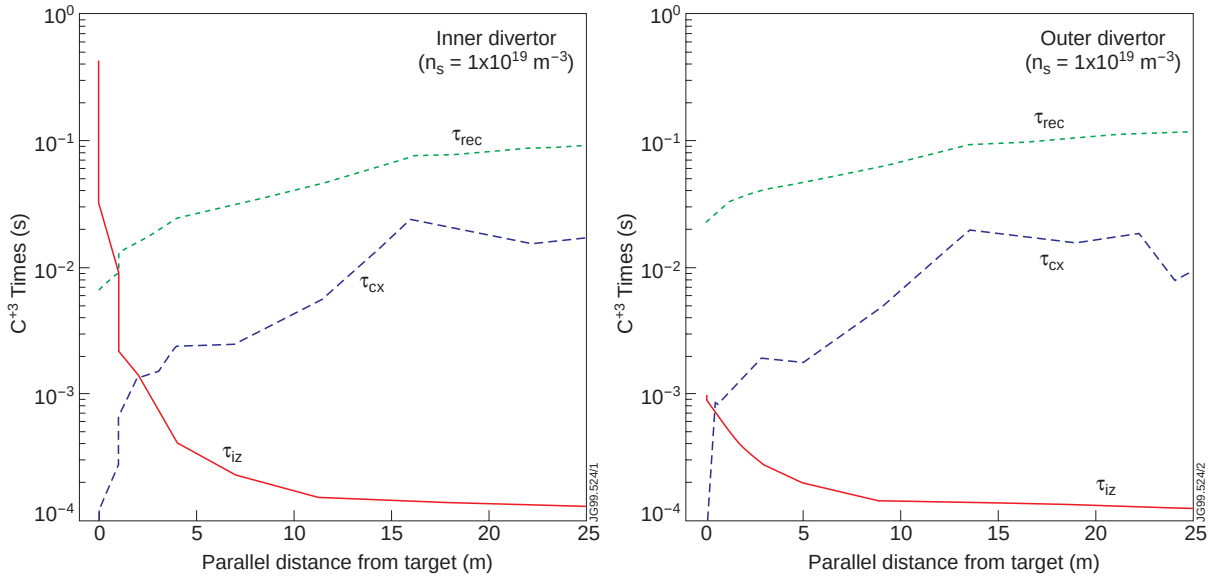

Figure 10. C^{+3} characteristic times for ionization, charge exchange and electron recombination along the separatrix in the inner (a) and outer (b) divertor region at low density (n_S = 1 x 10^{19} m^{-3}) for the pulse of Fig. 4.

At low density (n_S = 1 x 10^{19} m^{-3}) the lower charge states, C^{+1} and C^{+2}, are fully ionizing since the ionization time, τ_{iz}, is much smaller than both the charge exchange and the free electron recombination times, τ_{cx} and τ_{rec}. For example, for C^{+1} $\tau_{iz} \sim 10^{-5}$ s compared with $\tau_{rec} \sim 10^{-1}$ s < τ_{cx}~1-10s in both inner and outer divertor. Thus, including charge exchange in the model does not modify the ionization balance of the lower charge states at low density. The C^{+3} characteristic times are shown in Fig. 10 for the inner and outer divertor regions. It can be seen that in a small volume near the inner target plates $\tau_{cx} \leq \tau_{iz}$. However, this volume is too small for the C^{+2} density to be significantly modified by charge exchange even if the neutral deuterium and C^{+3} distributions overlap in this region (Fig. 11).

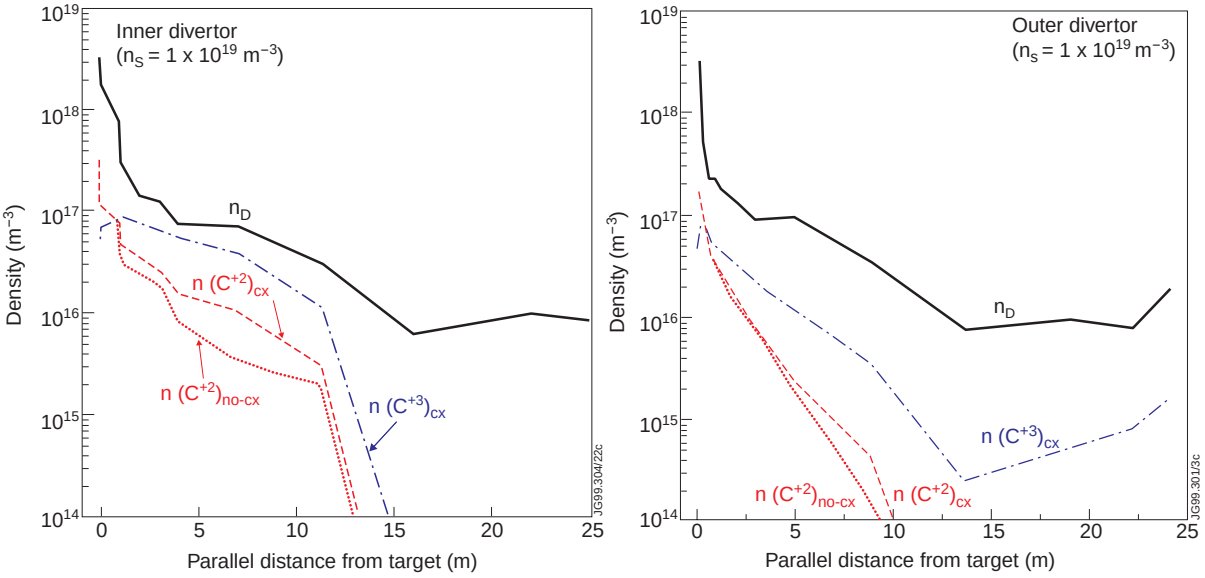

Figure 11. EDGE2D/NIMBUS calculations of neutral deuterium, C^{+3} and C^{+2} densitites (with and without charge exchange) along the separatrix in the inner (a) and outer (b) divertor region at low density (n_S = 1 x 10^{19} m^{-3}) for the pulse of Fig. 4.

The higher charge states, C^{+4} and C^{+5}, are fully recombining in the JET divertor even at low density, with $\tau_{cx} < \tau_{rec} << \tau_{iz}$. This is consistent with spectroscopic observations showing the lack of these ionization stages in the divertor region [1].

As the separatrix density is increased and the plasma evolves through the high recycling to the detached regime, the relative magnitude of the characteristic times varies also for the lower carbon charge states, mostly in the inner divertor region where the reduction in electron temperature is largest. At plasma detachment (n_S = 2x10^{19} m^{-3}) $\tau_{rec} < \tau_{iz} < \tau_{cx}$ for C^{+1} in the inner divertor. Therefore C^{+1} ions are lost through free electron recombination into neutral atoms. In the outer divertor τ_{iz} is the shortest characteristic time. For C^{+2} $\tau_{rec} < \tau_{cx} << \tau_{iz}$ in both divertor legs. For this reason the inclusion of charge exchange in the model does not modify the C^{+1} density distribution as shown in Fig.12 (a similar picture is obtained for the outer divertor).

The C^{+3} characteristic times for the detached solution are shown in Fig. 13. Since $\tau_{cx} < \tau_{rec} < \tau_{iz}$ both in the inner and outer divertor, the C^{+2} density may be modified when charge exchange is included in the model. However, due to the poor overlap between C^{+3}

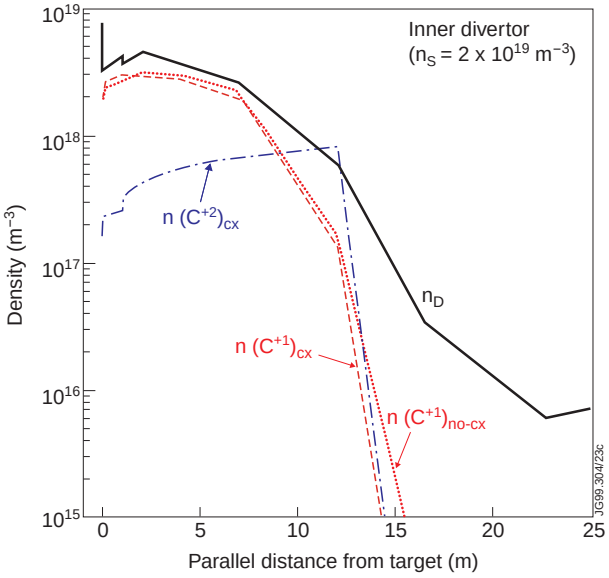

Figure 12. EDGE2D/NIMBUS calculations of neutral deuterium, C^{+2} and C^{+1} densitites (with and without charge exchange) along the separatrix in the inner divertor region at detachment (n_S = 2 x 10^{19} m^{-3}) for the pulse of Fig. 4.

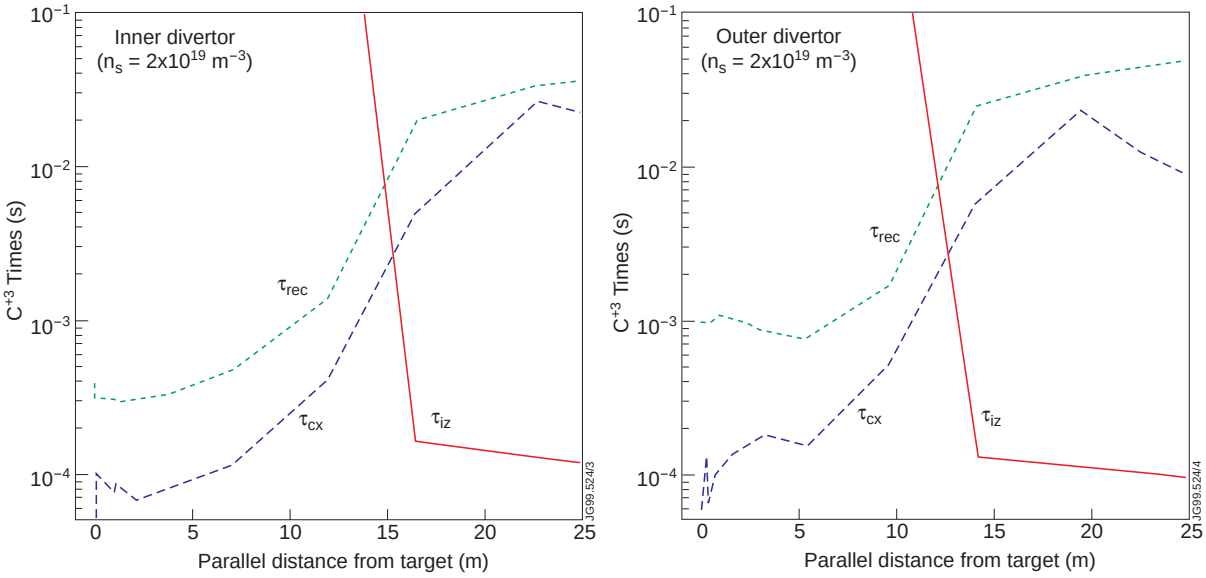

Figure 13. C^{+3} characteristic times for ionization, charge exchange and electron recombination along the separatrix in the inner (a) and outer (b) divertor region at detachment (n_S = 2 x 10^{19} m^{-3}) for the pulse of Fig. 4.

donor and D^0 distributions in the divertor region (see Fig. 14 for the inner divertor. A similar picture applies to the outer divertor) the C^{+2} density is unchanged.

Finally, charge exchange recombination into C^{+3} is negligible due to the lack of C^{+4} in the divertor volume, despite the C^{+4} characteristic times being $\tau_{cx} < \tau_{rec} << \tau_{iz}$.

To summarize, we find that carbon emission in the JET divertor region is weakly sensitive to charge exchange with deuterium neutrals. In addition, there is no clear correlation of the effect of charge exchange on carbon emission with increasing neutral density in the model.

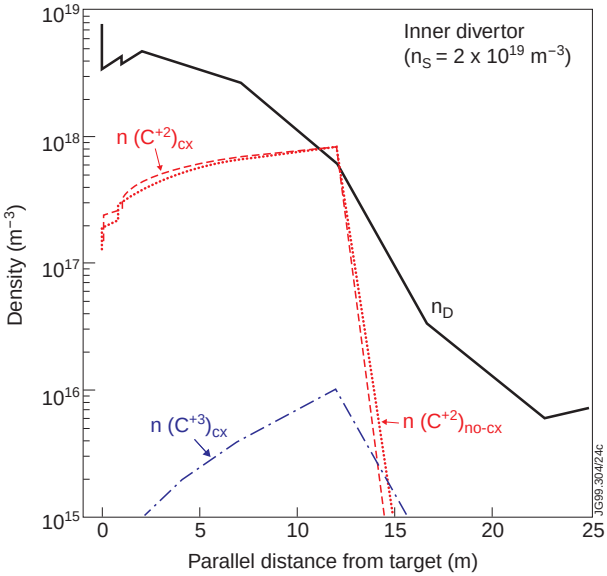

Figure 14. EDGE2D/NIMBUS calculations of neutral deuterium, C^{+3} and C^{+2} densitites (with and without charge exchange) along the separatrix in the inner divertor region at detachment (n_S = 2 x 10^{19} m^{-3}) for the pulse of Fig. 4.

4.3. Sensitivity to Parameters of the Transport Models

In order to test the robustness of the conclusion that charge exchange is not influential in the divertor as a mechanism to change the carbon impurity radiant losses, we have performed sensitivity tests on some parameters of the transport model. We examine the hypothesis that the weak sensitivity on charge exchange of the carbon density and radiation distributions in the

divertor is a consequence of the impurity transport model used in the simulations and that a different choice of transport coefficients may lead to a 'regime' where charge exchange plays a role.

In the momentum balance equation the total force on the impurity ions can be written as [11,12]:

$$F = m_Z\, v_Z\, dv_Z/ds = F_P + F_E + F_F + F_T + F_\eta \qquad (8)$$

where m_Z and v_Z are the mass and velocity of the impurity ion, F_P is the impurity pressure force, F_E is the electrostatic force on the impurities, F_F is the friction force between the impurity ions and the hydrogenic plasma flow, F_T is the thermal diffusion force, which arises due to the presence of electron and ion temperature gradients in the plasma flow and F_η is the viscous force. In the divertor the dominant forces are the friction force, which tends to drag the impurities towards the target plates, namely

$$F_F = m_Z\, (v_i - v_Z) / \tau_S \qquad (9)$$

where v_i is the velocity of the plasma ion flow and τ_S is the Spitzer slowing down time [13], and the thermal diffusion force, acting in the opposite direction, namely

$$F_T = \alpha\, dT_e/ds + \beta\, dT_i/ds. \qquad (10)$$

The coefficients α and β are given by Neuhauser et al. [14]. Our first sensitivity test therefore consists of varying the balance between friction and thermal force on the carbon ions and then re-assessing the effect of charge exchange.

Secondly, we note that one of the main uncertainties in divertor plasma models is the perpendicular transport coefficients. Our simulations were carried out assuming a constant perpendicular particle diffusion coefficient $D_\perp = 0.1\ m^2/s$. This value of $D_\perp$ enables us to match the measured ion flux profile to the divertor target. However, this coefficient is also assumed to be the same for both the hydrogenic *and* the impurity ions (all charge states). Our second sensitivity test therefore consists in varying $D_\perp$ for the carbon ions.

4.3.1. Sensitivity to Parallel Transport

We vary the force balance on the carbon ions substantially by varying the parallel thermal gradient force in the scrape-off layer. Starting from the detached EDGE2D/NIMBUS solution discussed in section 4.2, we first reduce the parallel thermal gradient force by a factor of 5 (and thus enhanced the parallel friction force on the impuritites). The resulting 2-D plasma solution is very similar to our original solution which assumes classical parallel transport. The simulated line of sight emissivities for the deuterium spectral lines are very close to those shown in Fig. 6. The C II line emission is also unchanged. The C III emission at 538 Å is reduced by 20% with this variation of the impurity parallel transport, while the visible line emission at 4650 Å is reduced by 30% in the inner divertor. The C IV VUV line emission is unchanged, while the 5810 Å line emission in the inner divertor is reduced by 40%. However, it is to be noted that in this

case the simulations with and without charge exchange give very similar results, except for the C IV line emissivities which are reduced by 20 to 30%, depending on the spectral line, when charge exchange is switched off.

A second test consists in increasing the parallel thermal force by a factor of 5 in the high density solution. We find no modification to the deuterium emission. Also the carbon line emission, both in the visible and VUV range, is essentially unaffected by the increase in the parallel thermal force at detachment, the largest variation from the initial solution being of order 20% in the C III VUV line emission. In this solution we observe very little difference in the simulations with and without charge exchange. The only notable effect is an enhancement in the C IV emission and in the C III visible emission by about 25-30% when charge exchange is included in the simulation. However, this is too small to be measured experimentally.

4.3.2. Sensitivity to Perpendicular Transport

We investigated the sensitivity of charge exchange on the variation of the perpendicular transport for carbon ions. We started with the high density solution ($n_S = 2x10^{19}$ m^{-3}) shown in Figs. 6-9 and varied the perpendicular diffusion coefficient for carbon ions, $D_\perp$, increasing it from its original value of 0.1 m^2/s to 0.5 m^2/s. We find that the deuterium spectral emission is unaffected by this change. On the other hand, there is some variation in the C III and C IV line intensities: a reduction of up to 30% in the C III VUV emission and an increase of a factor 2.5 in the 4650 Å line intensity in the outer divertor. The C IV VUV line emission increases by 40% and the intensity of the 5810 Å line increases by a factor 2.5 in the outer divertor.

We obtain a significant difference between the simulations with and without charge exchange only in the simulated C IV line intensities. The VUV line emission is a factor of 2 higher and the visible emission in the inner divertor is a factor of 1.6 higher when charge exchange is switched on. However, such enhancement in these C IV line intensities is not sufficient to modify appreciably the total carbon radiated power, since the intensity of the C IV resonance line (λ = 1549.1 Å) is not affected by the presence of charge exchange in the model.

5. CONCLUSIONS

Because of the increased neutral density in the divertor region as divertor plasma operation progressively moves towards high recycling and detached plasma regimes, it has been a general expectation that low energy charge exchange reactions with neutral deuterium can influence the ionization balance of impurities and selected spectral line emissions. In this paper we have assessed this topic quantitatively, by coupling charge exchange to divertor plasma and impurity transport modelling. We have focused on carbon ions, carbon being the main intrinsic impurity in the JET tokamak.

In the simulation of JET divertor discharges we have found that, even at high neutral deuterium concentrations, charge exchange recombination does not alter significantly the radiated power distribution of the main carbon radiators in the JET divertor, C^{+1} – C^{+3}. Spectral line

emission from these ions, both in the visible and VUV, is modified by at most 30-40% when charge exchange is included in the model. Larger changes in the impurity transport and steady state distributions are produced by variations of the divertor plasma profiles within their experimental uncertainties.

This weak sensitivity of the carbon ionization balance on charge exchange in divertor plasmas is explained by comparing the characteristic times of ionization, recombination and charge exchange for the different carbon impurity charge states. In the low recycling regime, the charge exchange times for C^{+1} – C^{+3} are comparable to or shorter than the free electron recombination times. However, the ionization times are significantly shorter, thus making the effect of charge exchange negligible. In high density, low temperature, detached plasmas free electron recombination determines the losses for the lowest charge states of carbon (C^{+1} – C^{+2}). C^{+3}, marking the balance between ionization and recombination losses, is potentially sensitive to changes in the radiation pattern induced by charge exchange. However, very little spatial overlap occurs between the neutral deuterium donor and recombining C^{+4} ion distributions in the divertor region. The ionization times of the higher charge states, C^{+4} - C^{+5}, are much larger than the corresponding recombination times in the divertor, which explains the small contribution to the total divertor radiation from these charge states.

We have reviewed and reassessed the low energy charge exchange cross section data in the literature. Using these data we have calculated total and state selective charge exchange recombination rate coefficients for all carbon ions, which are needed for ionization balance calculations and line emission modelling. These rate coefficients are now available in the ADAS database. All the charge exchange cross sections are for capture from the ground state of the recombining carbon ions. Extension of these data to include capture from metastable state of the recombining ions would be useful for divertor conditions, where the metastable populations of key carbon ions, such as C^{+2}, are comparable to or even greater than the ground state populations.

APPENDIX A. REVIEW OF LOW ENERGY CHARGE EXCHANGE CROSS SECTION DATA FOR CARBON IONS

In this review we have included both theoretical and experimental cross sections and established a preferred curve through the data for each carbon ion. We have then used these preferred data for the calculation of the collisional radiative charge exchange rate coefficients described in section 2.

Generally, total charge exchange cross sections are most readily available, but for some of the carbon charge state sparse at thermal energies. It was essential for the present work to be able to have also state selective charge exchange cross sections and so we gave preference to the sources who report state selective cross sections. We then assembled the total cross section curves from the sum of the state selective cross sections and finally compared these with other measured or calculated total cross section data in the literature.

Usually, the state selective cross section curves do not cover as wide a collision energy range as the total cross sections do (mostly at high energy). Although our main thrust is on charge exchange emission at thermal energies, our strategy has been to extrapolate the state selective cross section curves over the wider energy range of the total cross section. When the cross section fall-off at high energy is clearly established from the data we extrapolate at constant slope on a log scale, otherwise we extrapolate at constant fraction of the total cross section. In this way we ensure at least the correct high energy behaviour of the total cross section and limit the error from the high velocity contribution of the integrals in the calculation of the partial rate coefficients. Low energy extrapolation is discussed separately for each carbon charge state.

An important aspect of this review, which is targetted on divertor plasma studies, is that of metastable resolution of the cross section measurements and calculations. All cross section data reviewed below refer to capture from the ground state of the recombining carbon ion. In the cross section measurements, the fraction of metastable ions in the projectile beam is usually estimated to be negligible. The available theoretical calculations do not provide estimates of the charge exchange cross section for capture from metastable states of the recombining ion. On the other hand, over a large range of divertor plasma densities and temperatures the metastable population of some of the carbon ionization stages is significant. For instance, the C^{+2} ($2p\ ^3P$) metastable population density is 1.2 to 1.5 times that of the ground state in the temperature and density range T_e = 5 - 20 eV and $n_e = 10^{19} – 10^{20}$ m^{-3}. In this case, electron capture into C^{+1} may be underestimated when only capture from ground state C^{+2} ions is included in the rate coefficients. Clearly further experimental and/or theoretical alteration to such charge exchange cross sections is required to improve the accuracy of charge exchange modelling in edge/divertor plasmas.

A.1 $C^{+1} + H \rightarrow C^{+0} + H^{+}$

Our primary reference is the work of Stancil et al. [15], which reviews existing calculations and measurements of total cross sections for this reaction, as well as performing new ones in the collision energy range 10^{-3} - 10^{3} keV/amu. The authors propose a new preferred cross section curve for this reaction, which agrees well with that of Phaneuf/Janev [16] for energies greater than 400 eV/amu. At lower energies, in the approach to the threshold, the new calculations and measurements deviate strongly from the Phaneuf/Janev curve (see Fig. 15). Stancil et al. examine the reason for this large discrepancy between the older measurements of Nutt et al. (in ref. [17]), using merged beams, and their own measurements, also using merged beams, and molecular orbital close coupling (MOCC) calculations. They suggest that the most probable reason for the larger cross sections found by Nutt et al. is the contamination of the ion beam with metastable $C^{+1}(^4P)$ ions. However, this is not fully supported by the theoretical calculations of Stancil et al. When electron capture from the reaction:

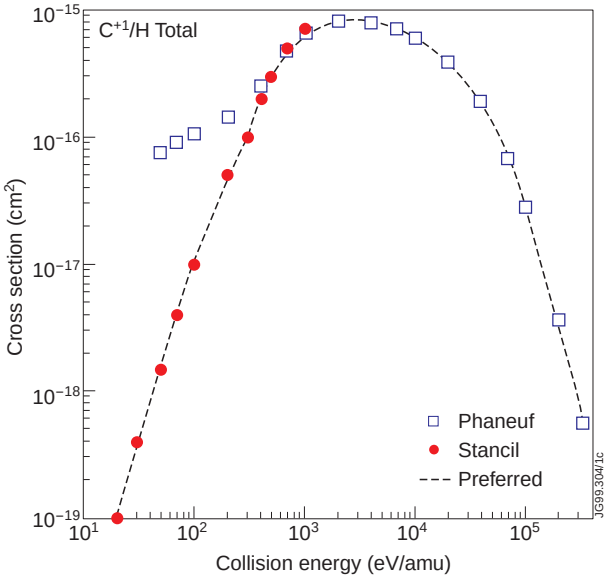

Figure 15. Total charge exchange cross sections for C^{+1}/H, showing the preferred curve of Janev and Phaneuf [16] and the more recent preferred curve of Stancil et al. [15] used in this work. The total electron capture is assumed to be into the ground state of C^{+0}.

$$C^{+1}\ (^4P) + H \rightarrow C^{+0} + H^{+} \qquad (11)$$

is added to capture from ground state $C^{+1}\ (^2P)$ the sum of the two remains significantly smaller than the measurements by Nutt et al. The uncertainty in the new recommended cross section curve is $\leq 25\%$ for $E > 1$ keV/amu, and ~ 100% at lower energy [15]. Since no state selective cross section data are available, we are obliged to assume electron capture to occur entirely into the $2p^2\ (^3P)$ ground state of neutral carbon. Therefore we use these data for ionization balance studies only and not for specific line emission simulations. Since C I is not an important radiator in JET divertor plasmas [1] this does not constitute a severe restriction for our study.

A.2. $C^{+2}(1s^2\ 2s^2\ ^1S) + H \rightarrow C^{+1}(1s^2\ nl\ n'l') + H^{+}$

Our primary sources are state selective cross section calculations from Heil et al. [18] and total cross sections from the ORNL compilation [17]. The state selective cross section data are only available for a limited energy range, 0.27 - 8.1 eV/amu, but suggest that electron capture into the ground state, $C^{+1}(2s^2\ 2p\ ^2P)$, is only important at low energies, although the cross section is

small and decreases with increasing energy. A second channel, $C^{+1}(2s\ 2p^2\ ^2D)$, becomes accessible and the dominant cross section at higher energies (see Fig. 16). At low energies the cross section is small and subject to large experimenatl uncertainties. Electron capture from metastable state ions $C^{+2}(1s^2\ 2s\ 2p\ ^3P)$ might also affect the total cross section, as shown qualitatively by the experiments of McCullough et al. [19] in the keV/amu energy range. The cross sections from Heil et al. are for capture from the ground state of C^{+2} ions only. Due to the lack of state selective cross section data for collision energies E > 8.1 eV/amu, we have assumed that for E> 8.1 eV/amu all electron capture occurs into the $2s\ 2p^2\ (^2D)$ state, while capture into $2s^2\ 2p\ (^2P)$ goes to zero, as shown in Fig. 16.

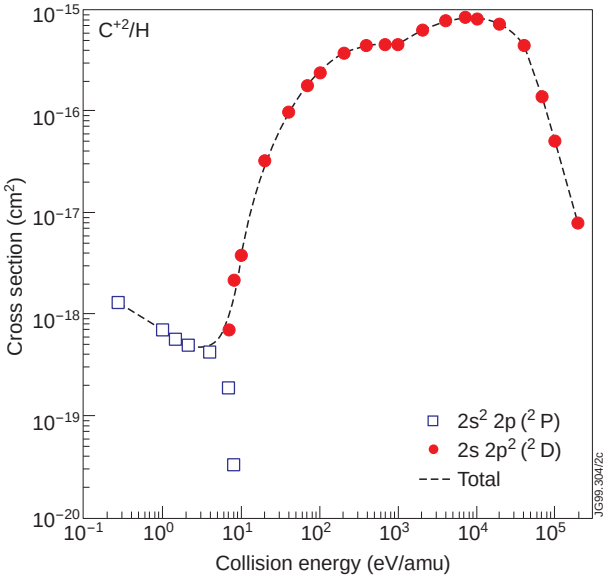

Figure 16. State selective [18] and total [17] cross section data for C^{+2}/H. For E > 8.1 eV/amu all capture is assumed into state $2s\ 2p^2\ (^2D)$.

A.3. $C^{+3}(1s^2\ 2s) + H \rightarrow C^{+2}(1s^2\ nl\ n'l') + H^+$

The most extensive sets of state selective charge exchange cross sections exist for this reaction, which extend to very low energies. Theoretical calculations based on the molecular orbital curve crossing model have been carried out by Blint et al. [20], Watson and Christensen [21], Heil et al. [22] in the thermal energy range. These calculations were motivated by astrophysical interest since the cross section for this reaction becomes very large in the few eV range. The calculations were later extended by Bienstock et al. [23] to energies up to 5 keV/amu. Opradolce et al. [24] performed molecular orbital calculations including translation factors in the energy range 10-5000 eV/amu, with both radial and rotational coupling. The work covered capture into triplet states only. Errea et al. [25] have calculated total and state selective cross sections for collision energies between 0.04 and 9 keV/amu. The calculations were performed using a 22-state molecular orbital calculation with a common translation factor. Herrero et al. have extended the work of Errea et al. to lower energies, providing total [26] and state selective [27] cross sections in the collision energy range 0.004 - 90 eV/amu. For this low energy range the authors adopted a quantal treatment of the molecular dynamics. Herrero et al. also performed calculations of cross sections for charge exchange with deuterium, in light of experiments carried out by Havener et al. [28] for this reaction. At very low energies these cross sections are found to be significantly smaller than those for H, owing to the dynamical effect of the reduced mass. At the lowest

energies considered (0.003 eV/amu), the cross sections for D can be as low as 50% of those for H, but this is not relevant to divertor plasma applications and so we adopt the cross section data for H. At energies E ? 0.1 eV/amu the D cross sections are practically identical to those for H.

Experimentally, state selective electron capture for this reaction has been investigated by Ciric et al. [29] from 0.7-4.6 keV/amu using photon emission spectroscopy and by McCullough et al. [19] from 0.6 to 18 keV/amu and by Wilkie et al. [30] in the 1.5 - 18 keV/amu energy range with higher energy resolution using translational energy spectroscopy. The measurements of Wilkie et al. do not resolve capture into 3d ^{1}D and ^{3}D states or into 3p ^{1}P and ^{3}P states, therefore these cross sections were not included in our review.

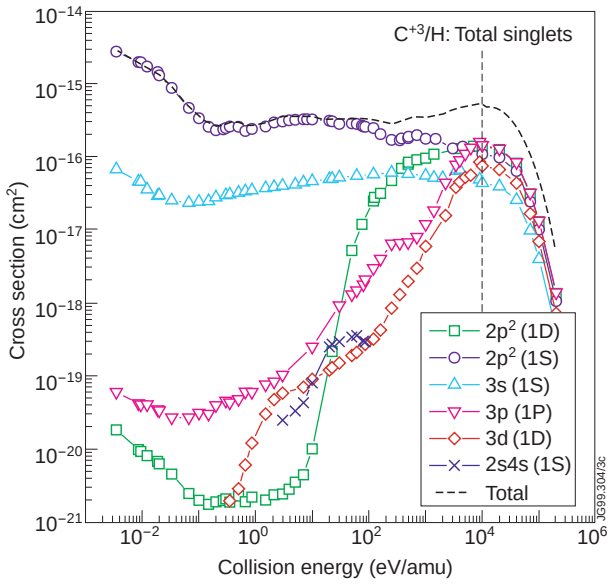

Figure 17. Preferred curves of C^{+3}/H state selective cross sections for capture into singlet states.

We summarize in Table 1 the sources of state selective cross section data for capture into the different final states of C^{+2}.

In the triplet manifold the dominant channel is capture into $C^{+2}(3s\ ^3S)$, while in the singlet manifold capture into $C^{+2}(2p^2\ ^1S)$ is the dominant channel at intermediate to low energies. This is shown in Fig. 17 and 18, where we plot our preferred curves for state selective cross sections for capture into singlet and triplet states of C^{+2} respectively. We have extrapolated these curves at high energy at a constant fraction of the total ORNL [17] curve.

The total cross section is dominated by the triplet component. The total cross sections (see Fig. 19), obtained by summation of the state selective cross sections shown in Fig. 17 and 18, have been compared with the ORNL preferred curve and with the measurement of total cross sections of Havener et al. [28]. These were obtained in the energy range 0.3 - 3000 eV/amu using merged beams, with the low energy measurements (≤560 eV/amu) performed with D instead of H.

Table 1. Summary of C^{+2} final states in C^{+3}/H charge exchange reactions for which state selective cross sections are available, and their sources.

C^{+2} Final State	Authors
$2p^2$ (^1S)	Herrero et al. [26], Errea et al. [25], Heil et al. [22], Bienstock et al. [23], Ciric et al. [29], McCullough et al. [19], Wilkie et al. [30]
$2p^2$ (^1D)	Herrero et al., Errea et al., Heil et al., Bienstock et al., Ciric et al., McCullough et al., Wilkie et al.
3s (^1S)	Herrero et al., Errea et al., Ciric et al.
3p (^1P)	Herrero et al., Errea et al., Ciric et al.
3d (^1D)	Herrero et al., Errea et al., Ciric et al.
4s (^1S)	Herrero et al.
$2p^2$ (^3P)	Herrero et al., Ciric et al.
3s (^3S)	Herrero et al., Errea et al., Heil et al., Bienstock et al., Opradolce et al., Ciric et al., McCullough et al., Wilkie et al.
3p (^3P)	Herrero et al., Errea et al., Heil et al., Bienstock et al., Opradolce et al., Ciric et al., McCullough et al.
3d (^3D)	Herrero et al., Errea et al., Ciric et al.
4s (^3S)	Herrero et al.

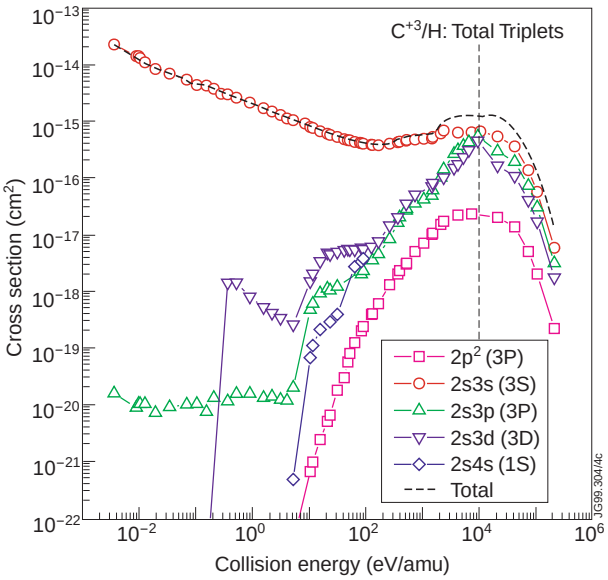

Figure 18. Preferred curves of C^{+3}/H state selective cross sections for capture into triplet states.

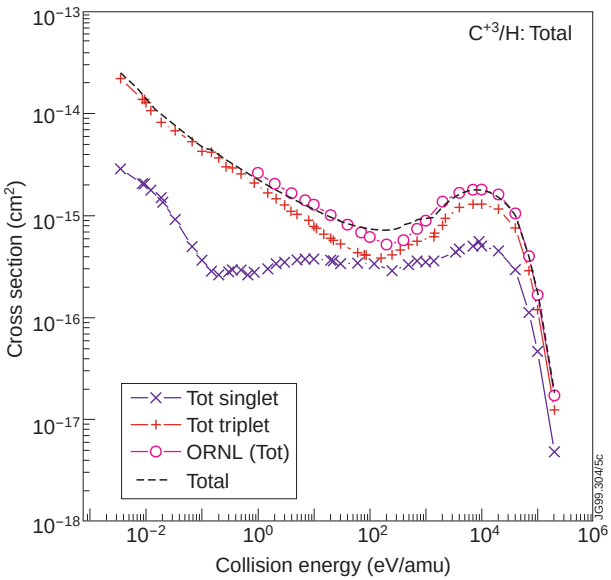

Figure 19. C^{+3}/H total cross sections.

A.4. $C^{+4}(1s^2) + H \rightarrow C^{+3}(1s^2\ nl) + H^+$

All the theories predict that the dominant electron capture occurs into the n = 3 levels of C^{+3} and that the contribution from other levels is small. This is confirmed experimentally. For state selective capture, references, on the experimental side, include measurements by Dijkkamp et al. [31] and Hoekstra et al. [32]. The measurements of Dijkkamp were obtained by photon emission spectroscopy using crossed beams in the collision energy range 1 - 6.6 keV/amu, while Hoekstra extended the measurements to lower energies (50 - 1330 eV/amu). On the theoretical side, Gargaud and McCarroll [33] calculated state selective cross sections for capture into n = 3 states using fully quantal molecular orbital calculations with a limited basis set (MO4) in the collision energy range 0.9 - 1180 eV/amu. Gargaud, McCarroll and Valiron [34] report molecular orbital calculations with an extended basis set (MO7) and including rotational coupling and electron translation factors in the energy range 0.9 - 1180 eV/amu. Fritsch and Lin [35] used a two center atomic-orbital (AO) expansion method in the energy range 0.1 - 20 keV/amu and report cross sections for capture into n = 3 and n = 4 states. The more recent calculations of Saha [36], in the energy range 20 - 1000 eV/amu, were performed using a semi-classical, impact parameter close coupling method based on a molecular description of the collision system and including translation factors. Total charge exchange cross sections for this reaction have also been measured by Bliek et al. [37] in the energy range 6 - 1000 eV/amu using merged beams. The total cross section, obtained as the sum of n = 3 and n = 4 state selective cross sections, was then compared to the recommended curve of Phaneuf [17]. The n = 3 state selective cross sections are shown in Fig. 20 together with our preferred curves. The latter are extrapolated at high energy to cover the same collision energy range of the total cross section curve. Below 200 eV/amu the measurements of Hoekstra et al. and the calculations of Fritsch and Lin show a faster decay of σ(3s) than the MO calculations. We have drawn our preferred curve between the two

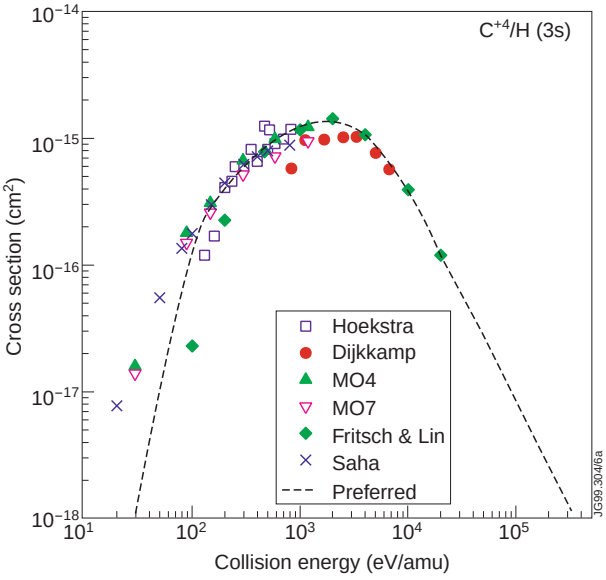

Figure 20 a. C^{+4}/H charge exchange cross section for capture into C^{+3}(3s).

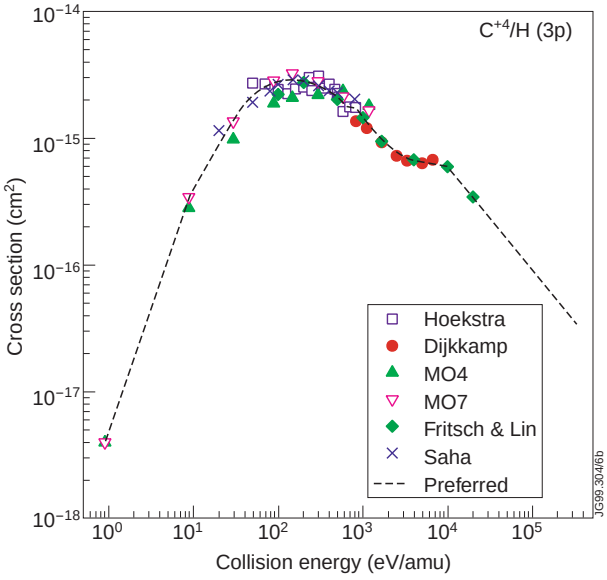

Figure 20 b. C^{+4}/H charge exchange cross section for capture into C^{+3}(3p).

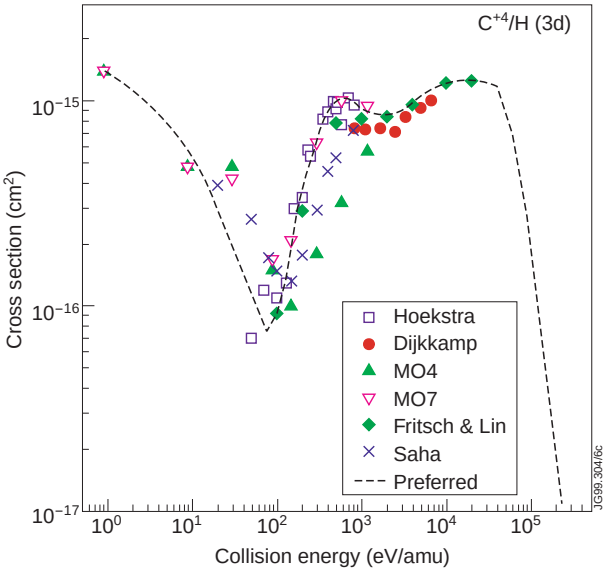

Figure 20 c. C^{+4}/H charge exchange cross section for capture into C^{+3}(3d).

groups of data extrapolating at constant slope. At high energy we follow the results of Fritsch and Lin and extrapolate above 20 keV/amu at constant slope. σ(3p) is the dominant cross section in the range 20-1000 eV/amu. At low energy C^{+4}/H charge transfer is dominated by capture into 3d. However, there is a certain scatter in the data for this reaction and the various sources show the minimum in the cross section at different collision energies. Since there are no measurements for this reaction below 50 eV/amu we follow the theory. The fall-off at high energy in the preferred curve is derived by extrapolation at constant fraction of the total cross section.

The total cross section is shown in Fig. 21. Also shown are the cross sections for capture into n = 3 and n = 4 states and the ORNL recommended curve. At higher energies (E > 1 keV/amu) capture into n = 4 states of C^{+3} cannot be neglected. We have prepared preferred curves through the measurements of Dijkkamp and the calculations of Fritsch and Lin in the energy range 0.5 - 20 keV/amu (not shown), extrapolating below 0.5 keV/amu with a rapid fall-off and above 20 keV/amu at constant fraction of the total ORNL cross section.

A.5. $C^{+5}(1s) + H \rightarrow C^{+4}(1s\ nl) + H^{+}$

The main reference is the work by Shimakura et al. [38], which provides theoretical state selective cross sections in the energy range 10 - 3000 eV/amu. The calculation used semiclassical close-coupling methods including 16 states and with translation factors. The dominant capture is into n = 4 states of C^{+4} ions at lower energies but at higher energies capture into n = 3 states is substantial. For the triplet manifold, C^{+4}(1s 4s) is the dominant cross section for electron capture below 500 eV/amu. Above this energy, the latter cross section rapidly decreases and the C^{+4}(1s 4d), C^{+4}(1s 4p) and C^{+4}(1s 3p) cross sections become important. For the singlet manifold, below 500 eV/amu the C^{+4}(1s 4s) and C^{+4}(1s 4f) cross sections are the main contributions to the total cross section. At higher collision energies the C^{+4}(1s 4d), C^{+4}(1s 3p) and C^{+4}(1s 3d) cross sections become increasingly important.

In Fig. 22 we compare the total cross section, derived by summation of the state selective cross sections of Shimakura et al., with the recommended total cross section curve of Phaneuf and Janev [17] in the energy range 1 – 10^5 eV/amu. We have extrapolated the cross sections of Shimakura et al. at low energy (1 < E < 10 eV/amu) and high energy (3 < E < 100 keV/amu) at

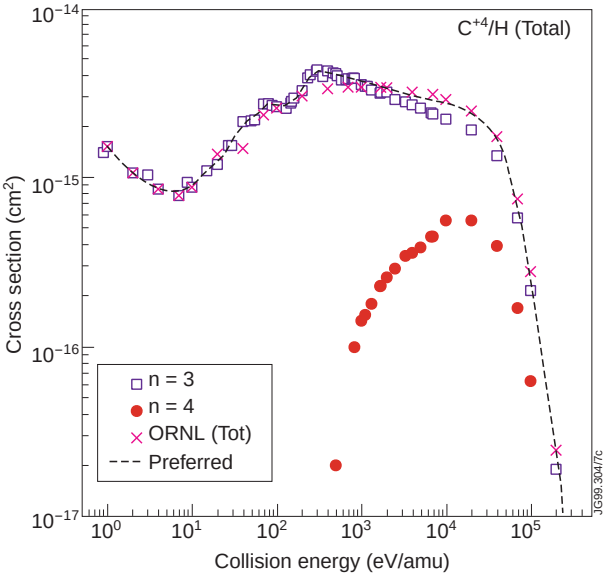

Figure 21. Total C^{+4}/H charge exchange cross sections.

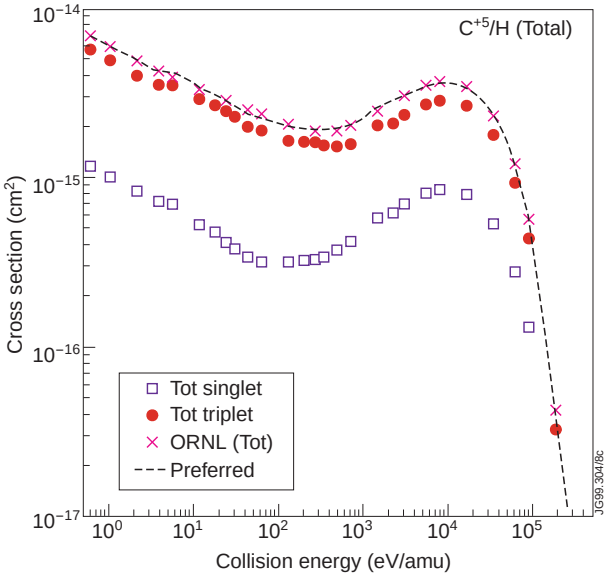

Figure 22. Total C^{+5}/H charge exchange cross sections.

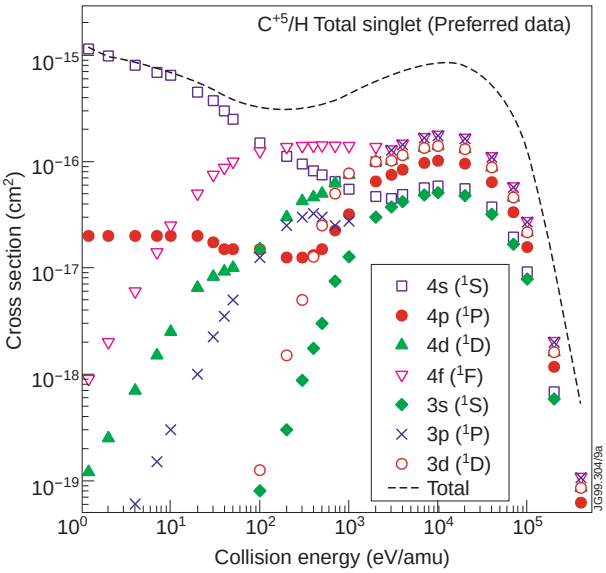

Figure 23 a. Total C^{+5}/H charge exchange cross sections for capture into the singlet manifold.

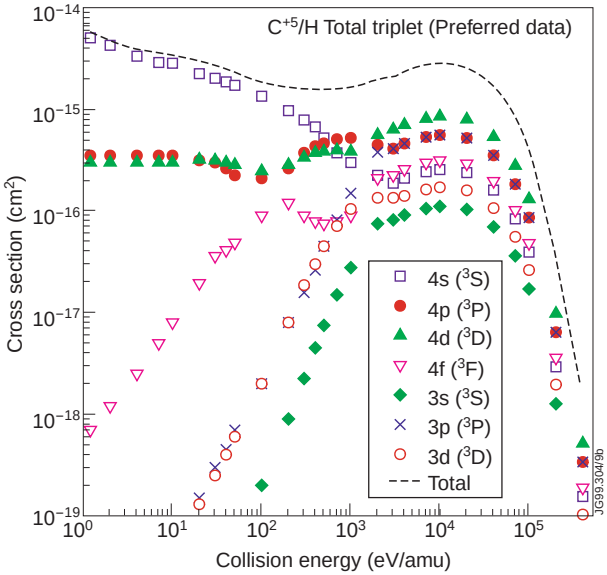

Figure 23 b. Total C^{+5}/H charge exchange cross sections for capture into the triplet manifold.

constant fraction of the ORNL recommended curve. In Fig. 23 we show our preferred curves for C^{+5}/H state selective cross sections for the singlet and triplet manifold respectively.

A.6. $C^{+6} + H \rightarrow C^{+5}(1s\ nl) + H^{+}$

For this reaction we have assembled n-shell total electron capture cross sections for the n = 4 and 5 shells of C^{+5} from the calculations of Green et al. [39], Fritsch and Lin [40], Kimura and Lin [41] and Macek and Dong [42]. Our population calculations use n-resolved rate coefficients for H-like carbon. The dominant channel is electron capture into n = 4 states of C^{+5} ions. Cross

sections for capture into n = 3 states are much smaller and of relevance only in the keV/amu energy range. They were not included in our state selective preferred curves. Green et al. used molecular orbital (MO) calculations to calculate nl state selective cross sections for capture into n = 4, 5 in the energy range 13 eV - 27 keV/amu. Fritsch and Lin calculated electron capture cross sections into n = 4, 5 l-subshells in the energy range 0.1-30 keV/amu using atomic orbital calculations (AO). Kimura and Lin used a unified treatment calculation, which combines the features of the AO and MO expansion, using the most suitable basis sets in each portion of the configuration space during the collision. Cross sections were calculated in the energy range 0.2-4 keV/amu. Macek and Dong calculated cross sections for capture into nl levels of C^{+5}, for n = 4, using a Landau-Zener model with rotational and degenerate Stark-effect coupling in the energy range 0.013 - 20.8 keV/amu.

The total cross sections from the different sources (except [42], which only reports cross sections for capture into n = 4) are in good agreement, as shown in Fig. 24, which shows also the recommended curve of Phaneuf and Janev [17]. However, the MO calculations of Green et al. predict more capture into n = 5 states than the AO and unified treatment calculations. This difference is largest (factor 6 – 10) in the 0.1 - 1 keV/amu energy range. Our preferred curve for the n = 5 cross sections follows the data of Fritsch and Lin and Kimura and Lin. The calculated cross sections for capture into C^{+5}(n = 4) from various sources are in good agreement, except for the calculations of Macek and Dong at energies < 200 eV/amu. Fig. 25 and 26 show C^{+6}/H charge exchange cross sections for capture into n = 4 and n = 5 respectively. We have extrapolated the state selective cross sections over the wider energy range covered by the ORNL recommended curve. Both at low and high energy the extrapolation was obtained at constant fraction of the total cross section.

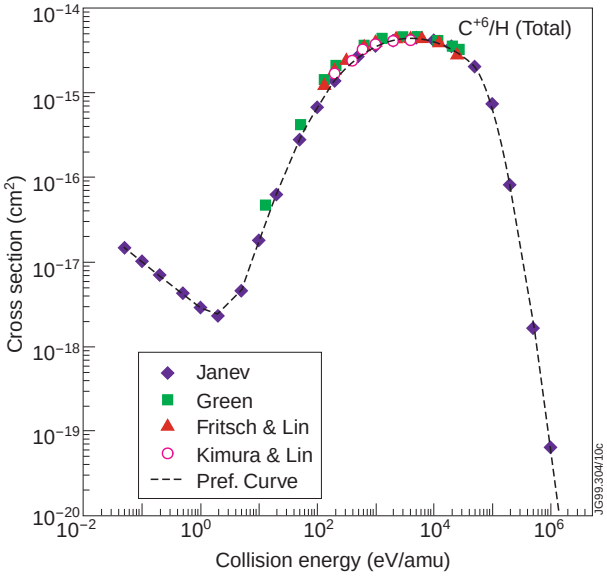

Figure 24. Total C^{+6}/H charge exchange cross sections.

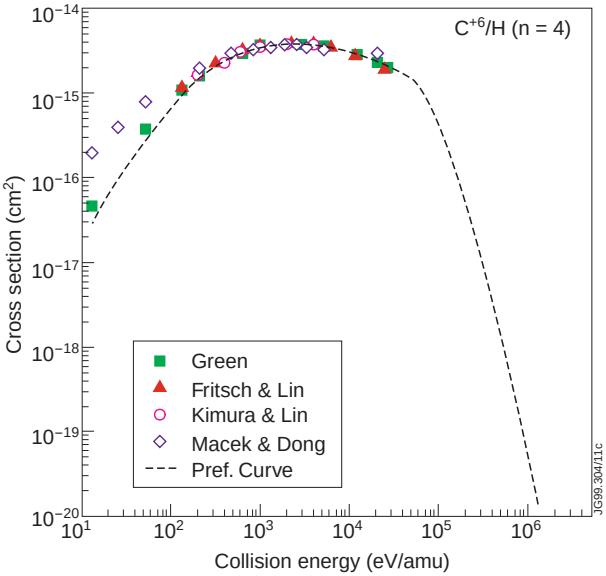

Figure 25. C^{+6}/H charge exchange cross sections for capture into n = 4.

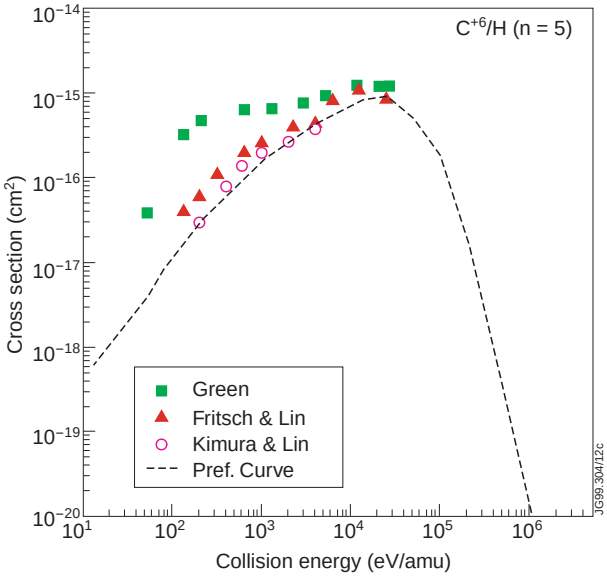

Figure 26. C^{+6}/H charge exchange cross sections for capture into n = 5.

ACKNOWLEDGEMENTS:

CFM wishes to thank Drs. G. Corrigan and J. Spence for their help with the EDGE2D/NIMBUS simulations. In addition, discussions with Dr. M. F. Stamp on the interpretation of the visible measurements are gratefully acknowledged.

REFERENCES:

[1] C.F. Maggi et al., J. Nucl. Mater. **241-243** (1997) 414.

[2] H.P. Summers, JET-IR(94)06 and http://patiala.phys.strath.ac.uk/adas/adas.html

[3] H.P. Summers and M.B. Hooper, Plasma Physics **25** (1983) 1311.

[4] R. Simonini et al., Contrib. Plasma Phys. **34** (1994) 448.

[5] S. I. Braginskii, Review of Plasma Physics **1** (1965) 205, Consultants Bureau, New York.

[6] A. Loarte et al., Nucl. Fusion **38** (1998) 331.

[7] R.D. Monk et al., Contrib. Plasma Phys. **36** (1996)37.

[8] G. M. McCracken et al., Nucl. Fusion **38** (1998) 619.

[9] C.F. Maggi, 'Measurement and Interpretation of Spectral Emission from JET Divertor Plasmas', PhD Thesis, University of Strathclyde, 1996. Also, JET-IR(96)05.

[10] W. Eckstein et al., Sputtering Data, IPP-9/82, 1993.

[11] P.J. Harbour and J. Morgan, Control. Fusion and Plasma Phys. 7D-II (1983) 427 (Proc. 11th EPS Conf., Aachen).

[12] P.C. Stangeby, Contrib. Plasma Phys. **28** (1988) 507.

[13] L. Spitzer, Physics of Fully Ionized Gases, Interscience Publishers, New York, 1962.

[14] J. Neuhauser et al., Nucl. Fusion **24** (1984) 39.

[15] P.C. Stancil et al., Astrophys. J. **502** (1998) 1006, and P.C. Stancil et al., J. Phys. B **31** (1998) 3647.

[16] R.K. Janev et al., At. Data Nucl. Data Tables **40** (1988) 240.
[17] R.A. Phaneuf et al., Atomic Data for Fusion, ORNL-6090, Vol 5, 1987.
[18] T.G. Heil et al., Phys. Rev. A **27** (1983) 2365.
[19] R.W. McCullough et al., J. Phys. B **17** (1984) 1373.
[20] R.J. Blint et al., Astrophys. J. **205** (1976) 634.
[21] W.D. Watson et al., Astrophys. J. **231** (1979) 627.
[22] T.G. Heil et al., Phys. Rev. A **23** (1982) 1100.
[23] S. Bienstock et al., Phys. Rev. A **25** (1982) 2850.
[24] L. Opradolce et al., J. Phys. B **21** (1988) 503.
[25] L.F. Errea et al., J. Phys. B **24** (1991) 4061.
[26] B. Herrero et al., J. Phys. B **28** (1995) 4607.
[27] B. Herrero, private communication, 1996.
[28] C.C. Havener et al., Phys. Rev. A **51** (1995) 2982.
[29] D. Ciric et al., J. Phys. B **18** (1985) 3629.
[30] F.G. Wilkie et al., J. Phys. B **19** (1986) 239.
[31] D. Dijkkamp et al., J. Phys. B **18** (1985) 4763.
[32] R. Hoekstra et al., Phys. Rev. A **41** (1990) 4800.
[33] M. Gargaud and R. McCarroll, J. Phys. B **18** (1985) 463.
[34] M. Gargaud et al., J. Phys. B **20** (1987) 1555.
[35] W. Fritsch and C.D. Lin, J. Phys. B **17** (1984) 3271.
[36] B. Saha, Phys. Rev. A **51** (1995) 5021.
[37] F.W. Bliek et al., Phys. Rev. A **56** (1997) 426.
[38] N. Shimakura et al., Phys. Rev. A **45** (1992) 7876.
[39] T.A. Green et al., Phys. Rev. A **25** (1982) 1364.
[40] W. Fritsch and C.D. Lin, Phys. Rev. A **29** (1984) 3039.
[41] M. Kimura and C.D. Lin, Phys. Rev. A **32** (1985) 1357.
[42] J. Macek and X.Y. Dong, Phys. Rev. A **40** (1989) 85.